ELSEVIER

Chemical Engineering Journal 137 (2008) 686–702

Chemical Engineering Journal

www.elsevier.com/locate/cej

Preparation and characterization of nanocrystalline, high-surface area Cu–Ce–Zr mixed oxide catalysts from homogeneous co-precipitation

Florian Huber[a,1], Hilde Venvik[a,*], Magnus Rønning[a], John Walmsley[b], Anders Holmen[a]

[a] *Department of Chemical Engineering, Norwegian University of Science and Technology (NTNU), N-7491 Trondheim, Norway*
[b] *SINTEF Materials and Chemistry, N-7465 Trondheim, Norway*

Received 12 February 2007; received in revised form 30 June 2007; accepted 6 July 2007

Abstract

$Cu_{0.23}Ce_{0.54}Zr_{0.23}$-mixed oxides were prepared by homogeneous co-precipitation with urea. The resulting materials exhibit high-surface area and nanocrystalline primary particles. The material consists of a single fluorite-type phase according to XRD and TEM. STEM–EDS analysis shows that Cu and Zr are inhomogeneously distributed throughout the ceria matrix. EXAFS analysis indicates the existence of CuO-like clusters inside the ceria–zirconia matrix. The pore structure and surface area of the mixed oxides are affected by preparation parameters during both precipitation (stirring) and the following heat treatment (drying and calcination). TPR measurements show that most of the copper is reducible and not inaccessibly incorporated into the bulk structure. Reduction–oxidation cycling shows that the reducibility improves from the first to the second reduction cycle, probably due to a local phase segregation in the metastable mixed oxide with gradual local copper enrichment during heat treatment.

Keywords: Homogeneous alkalinization; Urea hydrolysis; Solid solution; Cu–Ce–Zr mixed metal oxide; Reducibility; Drying; Surface-to-volume ratio

1. Introduction

1.1. Cu–Ce–Zr mixed metal oxides (MMO)

Mixed metal oxides (MMO) containing copper, cerium and zirconium are applied in several areas of heterogeneous catalysis. Ce–Zr mixed oxides are extensively used in three-way catalysts [1a,2]. Cu–Ce–Zr-based mixed oxides are applied within the field of hydrogen production: water-gas shift [3–5], steam reforming of methanol [6–9] and selective oxidation of CO [10–17]. In addition, they are used as NO reduction catalysts [18], for oxidation of methane [19,20], wet oxidation of phenol [21] and acetic acid [22], methanol synthesis [23,24], direct oxidation of hydrocarbons in solid-oxide fuel cells (SOFC) [25–27], and storage of reactive hydrogen for alkadiene hydrogenation [28].

Copper – in its reduced state – is typically regarded as the active catalyst component in MMO materials (except for SOFCs, where copper the main function is electronic conductivity [25]). Ceria acts as a reducible oxide support, enhancing the catalytic activity via metal–support interaction and/or improved dispersion of the active metal component [7,29]. An important property of ceria is the oxygen storage capacity (OSC), i.e. the ability to adsorb and release oxygen under oxidizing and reducing conditions, respectively, according to the reaction [30]:

$$CeO_2 \underset{\text{ox.}\ (H_2O/CO_2)}{\overset{\text{red.}\ (H_2/CO)}{\rightleftharpoons}} CeO_{2-x} \qquad (1)$$

In addition, ceria is found to stabilize the catalyst against deactivation [7,29] due to a higher thermal stability and/or better dispersion of the active metal. ZrO_2 is also known to improve the activity and stability of MMO-based catalysts [8,31]. Zirconium added to ceria to form Ce–Zr mixed oxides inhibits the thermal sintering of CeO_2 [2,30,32,33]. Incorporation of Zr into the ceria lattice enhances the reducibility of ceria [34–36], which may improve the catalytic activity of MMO catalysts relative to single oxides [37,38]. The amount of Zr dopant also affects surface area and crystallite size of the MMO [37,39], in conjunction with the calcination temperature [40]. In addition to its presumed function as an active catalytic species, Cu as a dopant in the fluorite lattice is found to improve the reducibil-

---

[*] Corresponding author. Tel.: +47 73592831; fax: +47 73595047.
E-mail address: Hilde.Venvik@chemeng.ntnu.no (H. Venvik).

[1] Present address: Haldor Topsøe A/S, Haldor Topsøe Research Laboratories, Nymøllevej 55, DK-2800 Kongens Lyngby, Denmark.

1385-8947/$ – see front matter © 2007 Elsevier B.V. All rights reserved.
doi:10.1016/j.cej.2007.07.025

ity of ceria [41,42], and affect particle size and surface area [24,43].

The activity and stability of MMO catalysts therefore depends on the interaction between the single components, for which a homogeneous distribution of the components throughout the material without pronounced segregation is a pre-requisite. The catalytic activity often scales proportionally with the surface area of the active components [4,44] since the reaction takes place at the surface of the catalyst. A homogeneous distribution of the components and a high-surface area of the material have to be assessed simultaneously during catalyst preparation.

Co-precipitation of metal (hydrous) oxides in aqueous solution at high pH has successfully been applied for preparing different metal oxide catalyst formulations. It has been stated that co-precipitation results in more active and stable catalysts than impregnation methods [17,20,45–47], because of a more homogeneous distribution of the elements. For impregnation–deposition methods, the interaction between the different components depends on the surface area of the support material and the amount of material impregnated or deposited. The existence of separate phases at higher loadings is likely [4].

1.2. Homogeneous co-precipitation with urea (HCP)

Homogeneous alkalinization via urea hydrolysis is an efficient co-precipitation procedure for preparation of MMO with high-surface area and well-defined particle size and shape [3,19,48–51]. Urea decomposes at elevated temperatures in a two-step reaction releasing ammonium and carbonate ions into the metal salt solution accompanied by a simultaneous increase in pH, which leads to the precipitation of basic carbonates [48,50,52]:

$$CO(NH_2)_2 + 2H_2O \rightarrow 2NH_4{}^{+} + CO_3{}^{2-} \qquad (2)$$

The decomposition rate strongly depends on the temperature [52], the rate constant increasing by a factor of about 200 as the temperature increases from 60 to 100 °C [50,52]. The kinetics of the metal ion hydrolysis, and hence the nucleation rate, can be tuned through controlled release of hydroxide ions to obtain well-defined particle shapes with a narrow particle size distribution [48–50]. Constant-pH co-precipitation procedures with other hydroxide ion sources, such as NaOH, are claimed to facilitate stronger agglomeration of primary particles into irregularly shaped clusters, resulting in a broader particle size distribution [50,51].

In terms of synthesizing MMO solid solutions, co-precipitation in general has to be regarded as a heterogeneous process. Because of different hydrolytic properties of the metal ions in aqueous solution, simultaneous nucleation is rarely the case. A phase containing only one cation usually nucleates to serve as site for the heterogeneous nucleation of a second solid. Further growth proceeds incorporating both cations at different rates [49]. As a result, the internal local composition of such composites usually varies from the centre to the periphery of each particle [48]. The detection of a homogeneous solid solution inside the MMO material depends on the characterization technique used. The detection of single-phase MMO by conventional XRD techniques does not exclude the presence of nanodomains of single-component-rich phases [2], since XRD averages properties over a macroscopic scale as well as being insensitive to amorphous phases and ordered structures below about 2 nm [53,54].

1.3. Effect of synthesis parameters

Synthesis parameters that may affect the resulting catalyst material properties such as surface area, particle size and morphology are [21,48,50]: type of precursor salt, organic additives (from simple organic solvents to surfactants), total metal concentration, ratio between the metals in solution, urea concentration, procedure of urea addition (at ambient or high temperature), pH, procedure of mixing, synthesis temperature, aging time and post-treatment (drying and calcination conditions).

Nitrate precursor salts can easily be decomposed (an exothermic reaction), are inexpensive and have high solubility in aqueous media. Sulphates and chlorides are usually excluded since their residue in the catalyst material might accelerate catalyst deactivation [57,58]. The type of anion present in the solution can, however, have an impact on the precipitated particles [48].

The urea concentration (and initial ratio of urea to total metal in the solution), synthesis temperature and initial ratio between the metals in solution can affect the pH evolution rate, and hence the nucleation and growth. Small particles with a narrow particle size distribution have been obtained for high urea–total metal ratio and high reaction temperature [48,50]. Total metal concentration and acidic/basic additives affect pH and hence actual metal contents and phases present in the final product [48,49]. A high total metal concentration in the solution may result in enhanced particle agglomeration that reduces the surface area [48]. The aging time can affect crystallinity, particle size [50] and phase changes [49–59] and influence the final metal content [48,49]. All the parameters mentioned in this paragraph affect the nucleation and growth of mixed metal (hydrous) oxides/carbonates at different stages in aqueous solution, and may be highly correlated.

The effect of calcination temperature is well established for ceria-based systems. As for many systems, the particle size generally increases with a corresponding decrease in the surface area with increasing calcination temperature. As a consequence, the oxygen storage capacity of ceria and the catalytic activity of the material decrease [4,21,33,40,43,60–63].

There appears to be an optimum range for the metal loading of ceria-based mixed oxides, irrespective of preparation method [20]. The best redox properties and highest OSC for Ce–Zr solid solutions have been obtained within the range $0.2 \leq x \leq 0.4$, where x is the atomic fraction of Ce atoms replaced by Zr relative to pure CeO_2 [1b]. A maximum activity for water-gas shift [38] and for CO_2 reforming of methane [64] on Ce–Zr supported Pt catalysts was found with $x = 0.5$. A maximum methanol decomposition activity was reached at $x = 0.3$ for a Pd–Ce–Zr system [37]. For the same components, a maximum at $x = 0.2$ was found for CO and C_3H_8 oxidation [40].

A roughly linear relationship between the rate constant and Cu content up to 20 at.% was found for Cu–Ce mixed oxide catalysts for wet oxidation of phenol [21]. During selective CO oxidation over Cu–Ce catalysts, the highest reaction rate was obtained for a Cu content of 14 at.% as compared to 7 and 21 at.% [15]. This catalyst was also the one exhibiting the highest surface area. For the same reaction, catalyst system and preparation method, albeit higher surface areas, Kim and Cha [12] obtained the highest activity at 20 at.% Cu as compared to 10 and 50 at.%, but state that the difference between the three catalyst formulations is not large. Tang et al. [17] reported the CO conversion at low temperatures to be higher for 24 at.% Cu than for 7 and 13 at.% Cu in co-precipitated catalysts. In methanol steam reforming over Cu–Ce catalysts, the highest methanol conversion was observed for about 50 at.% Cu [46]. The maximum TOF was obtained for about 10 at.%. Shen et al. [24] found the initial maximum space–time yield in the methanol synthesis for 47 at.% Cu, but after about 25 h on stream the maximum shifted to the Cu–Ce catalyst with 23 at.% Cu. The difference between the 12, 23 and 47 at.% catalysts decreased with time on stream. For oxidation of CO and CH_4 over Cu/ZrO_2, the catalyst containing 20 at.% Cu in ZrO_2 was found to be most active [65]. Kundakovic and Flytzani-Stephanopoulos [19] achieved higher methane oxidation reaction rates for 15 at.% than for 5 at.% Cu in a Cu–Ce–La catalyst containing 4.5 at.% La. For the water-gas shift reaction, the highest CO conversion was measured for 15–20 at.% Cu in Cu–Ce–La catalysts containing 10 at.% La, but the difference is not large between catalysts with 5–40 at.% under the reaction conditions used [3]. In a more recent study of the same system [5], a 10 at.% Cu catalyst was found to perform slightly better than 5 and 15 at.% catalysts, and all were better than a 40 at.% catalyst. All these catalysts contained 8 at.% La in ceria, and the reaction conditions were similar in the two studies. Investigating the impact of the third metal component, they observed increased activity in the order 30 at.% La > 24 at.% Zr > 8 at.% La, and conclude that this effect is of chemical origin and not scalable with the surface area [5]. An improvement in the long-term stability and suppressed CO formation during methanol steam reforming over Cu–Ce–Zr catalysts by increasing the amount of Cu from 4 to 12 at.% has also been reported [66]. No significant enhancement was observed above 12 at.%, and this could be related to the detection of a separate CuO phase for samples with higher loading. The molar composition (Cu:Ce:Zr) of the 4 and 12 at.% catalyst were 4.4:51.0:44.6 and 12.1:44.3:43.6, respectively. Usachev et al. [14] achieved the best selectivity for selective oxidation of CO in excess hydrogen on Cu–Ce-based catalysts for Cu:Ce:Zr = 0.23:0.54:0.23. Interestingly, an optimum composition for Co–Ce–Zr catalysts for hydrogen production by ethanol steam reforming was found at Co:Ce:Zr = 0.225:0.500:0.275 [67].

Qualitative conclusions that can be drawn from the brief literature review above with regard the Cu–Ce–Zr composition are

(1) A Ce:Zr ratio between 3:1 and 2:1 appears to be a reasonable choice.
(2) The optimum amount of copper incorporated into the ceria structure lies in the range 10–20 at.%, probably limited by the amount of Cu that can be dispersed in ceria (or zirconia) without forming separate CuO phases.
(3) In three-component-mixtures, good performance is achieved with 40–50% of the Ce atoms replaced by Cu and Zr in equimolar amounts, i.e. an atomic ratio Cu:Ce:Zr ≈ 1:2:1.

The studies suggest that the catalytic properties of these MMO are insensitive to variations in the Cu content within a range of 10–25 at.%. In a study dealing with the preparation method, an experimental optimization of the composition may thus not be first priority, and reasonable values taken from literature should be adequate. An optimization of the metal composition has to be established for the specific application under relevant reaction conditions.

When using urea for precipitation of copper salts, the ammonia complexes (NH_4^+/NH_3) released during urea decomposition (Eq. (2)) interact with copper ions to form the deep blue copper–ammonia complex cations, $[Cu(NH_3)_4]^{2+}$ or $[Cu(NH_3)_6]^{2+}$, depending on the ammonia concentration. These complexes retain the copper ions in solution and decrease the amount of Cu in the final mixed metal precipitate. In a closed system (reflux conditions), an equilibrium will be established between precipitated copper hydroxide–carbonate phases and complex copper ions in solution. In an open system, this equilibrium can be shifted in favour of copper precipitation by releasing ammonia into the gas phase at elevated temperatures.

1.4. Description of the surface area of MMO

When characterizing the surface area of a certain material, the interesting parameter is the surface-to-volume ratio (stv, m^2/m^3), i.e. the fraction of the material exposed to the surrounding gas. The BET-deduced surface area (m^2/g) is useful for comparison of solids of equal composition. For materials with varying composition, however, the effect of the density has to be taken into account [68]. If the structure remains more or less unaffected by varying composition, the molar mass can simply be used to eliminate the mass effect, resulting in a mole-based BET value (m^2/mole). The BET results obtained by Kapoor et al. [37], for mesostructured Ce–Zr mixed oxides, and Hirano et al. [39], for non-ordered microporous Ce–Zr mixed oxides, are useful for exemplifying the effect of the metal composition on the surface area (Fig. 1). The stv (m^2/m^3) curves show the true impact of varying metal composition on the surface area of the materials. The densities used to calculate the stv from the BET data are based on a linear combination of tabulated values. The use of measured densities in such evaluations would further increase the precision. Comparing the surface-composition dependence for the specific BET (m^2/g) and the mole-based BET (m^2/mole) indicates the impact of the change in molar mass (with varying metal composition) on the BET surface-composition dependence. Comparing the surface-composition dependence for mole-based BET and stv shows the impact of the change in lattice spacing (with varying metal composition)

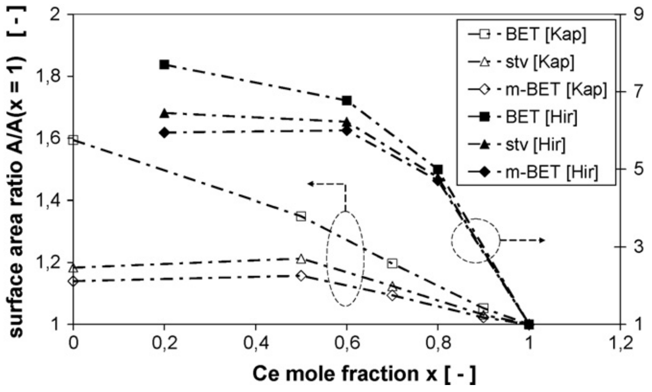

Fig. 1. Effect of material density and composition on BET data on Ce—Zr mixed oxides. Reported in the literature [37,39]. The surface area data of Kapoor et al. [37] (left axis) and Hirano et al. [39] (right axis) are given as surface area ratio normalized with the values of the pure CeO_2 samples (Ce mole fraction $x = 1$). M-BET denotes the BET surface area normalized with the molar mass (m^2/mole). The surface-to-volume ratio (stv, m^2/m^3) is calculated using densities based on a linear combination of tabulated values [100] for CeO_2 (7650 kg/m^3) and ZrO_2 (monoclinic for pure ZrO_2: 5680 kg/m^3, tetragonal for Ce—Zr mixed oxides: 6100 kg/m^3, according to the Ce—Zr phase diagram [1c,2,30]).

on the mole-based BET surface-composition dependence. In this simplified re-evaluation, the effect of a change in lattice spacing and hence the volume of the crystal unit cell by varying the metal composition affects the BET surface area only to a minor degree. A considerable contribution to the change in specific BET surface area with variation of the metal composition arises from the different molar mass of cerium and zirconium.

The effect of copper loading on the surface area of Cu–Ce mixed oxides can be evaluated in a similar way, for example by using data from Refs. [24] and [43]. Here, however, the surface area decreases with increasing Cu loading after an initial strong increase at very low Cu level. These curves (not shown) contain local minima and maxima, and the overall trend depends on the resolution of the experimental points. The same might be true for the Ce–Zr system. The BET data obtained for a series of co-precipitated Cu–Zr mixed oxides can be used in a similar way to evaluate these binary MMO [69].

1.5. Aim of the study

The aim of the present study is to determine relevant material properties of Cu–Ce–Zr mixed oxides prepared by homogeneous co-precipitation. This includes the actual catalyst composition relative to the nominal composition, as well as particle morphology, surface area, pore structure, metal distribution or degree of homogeneity, local atomic structure, and finally redox behaviour.

The initial concentration of the metal salts in aqueous solution (= nominal MMO composition) is kept constant. The nominal molar metal ratio used is: Cu:Ce:Zr = 0.23:0.54:0.23. This ratio is based on the literature, as described above. The parameters studied, in terms of their effect on surface area/particle size and pore structure, are: synthesis set-up with (a) two types of stirring/heat transfer configurations and (b) reflux conditions versus open system, drying conditions and heating rate during calcination.

An elementary analysis of the actual catalyst composition is carried out with inductively coupled plasma atomic emission spectroscopy (ICP-AES). Morphology and particle shape are examined with transmission electron microscopy (TEM). The particle size of the MMO is estimated with X-ray diffraction (XRD) and TEM. The homogeneity of the MMO is investigated using XRD (phase identification) and scanning-TEM (STEM, mapping of metal composition on a nm-scale). X-ray absorption spectroscopy (XAS) has been applied for elucidation of the oxidation state of bulk copper and its local environment (first coordination shell). The redox behaviour is characterized by means of temperature-programmed reduction and oxidation (TPR-TPO) cycles. The pore structure of the MMO is deduced from nitrogen adsorption–desorption isotherms. The specific surface area is estimated by the Brunauer–Emmet–Teller (BET) method.

2. Experimental

2.1. Synthesis

Copper(II)–nitrate–trihydrate (>99%), cerium(III)–nitrate–hexahydrate (>99.5%) and zirconyl(IV)–nitrate–hydrate (>99.5%) were purchased from Acros Organics. Urea (>99.5%) was purchased from Merck. Ethylene glycol (EG) (>99.5%) was purchased from Fluka. Ethanol was purchased from Arcus. All chemicals were used as-received. Deionised water was used for all catalyst preparations.

The two different set-ups used for catalyst preparation are shown in Fig. 2. The first set-up consists of a hot plate equipped with a magnetic stirrer (Fig. 2A). The precursor solution is stirred in a 600-ml glass beaker with a magnetic stirring bar rotating at approx. 1200 rpm. The temperature of the mixture is monitored with a thermometer immersed in the solution. This set-up is operated in an open mode, i.e. water evaporating during operation is compensated by continuous refilling. The glass beaker is partly covered to limit the evaporation. The second set-up consists of a 500-ml five-neck glass flask immersed in a stirred oil

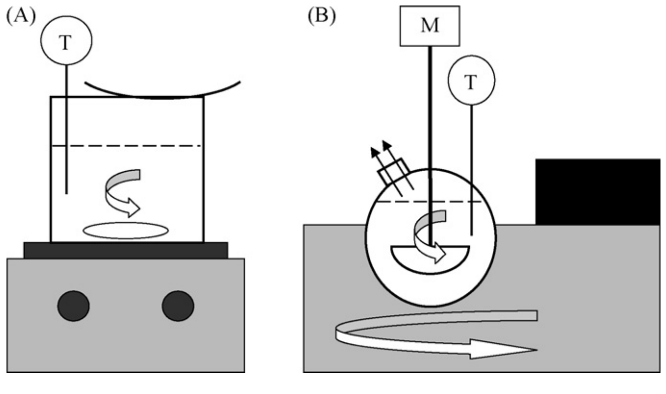

Fig. 2. The two different set-ups used for catalyst preparation. (A) Hot plate equipped with a magnetic stirrer and (B) 500 ml five-neck glass flask stirred with a blade agitator and immersed in a stirred oil bath.

bath (Fig. 2B). The temperature is monitored with an immersed thermometer, and the aqueous mixture is stirred with a blade agitator at approx. 750 rpm. In the closed mode, a reflux condenser is connected to the flask, and the unused flask necks are plugged. In the open mode, the three unused flask necks are left open to allow the evaporation as well as the continuous refilling of water.

A total amount of 0.1047 mole of Cu-, Ce- and Zr-salt (nominal composition: Cu:Ce:Zr = 0.23:0.54:0.23) were dissolved in 450 ml of water at ambient temperature. 0.9037 mole of urea were then added to the solution. After all solid components were dissolved to give a pH of approx. 1.8 at 20 °C, the light blue, transparent solution was placed on the hot plate/in the hot oil bath and heated up to 95 °C (unless otherwise noted) under stirring. It took about 30 min to reach the final temperature for both set-ups. The mixture was kept on the hot plate/in the oil bath for a period of 8 h, including precipitation and aging. The precipitation started after approx. 30 min in both set-ups. The colour of the suspension then changed from light blue to green over the next 45 min and then remained unchanged for the rest of the time. In the open mode, water at ambient temperature was added continuously to the suspension to compensate the evaporation. Ethanol was added instead of water in a single experiment, and in total 1.5 l of ethanol was added during synthesis.

The suspension was removed from the hot plate/oil bath after 8 h, and cooled to room temperature using water. The solid precipitate was filtered off and washed twice with 200 ml of deionised water (40–50 °C) under stirring (20– 30 min). Finally, the precipitate was dried (about 11 h at 100 °C, unless otherwise noted) and calcined in a muffle furnace for 2 h at 350 °C, either by placing the sample directly into the hot furnace (normal method) or by increasing the calcination temperature at 2 °C/min up to 350 °C.

In two preparations, an ethylene glycol–water mixture (18 mole% or 40 vol.% EG) was used instead of pure water, thereby increasing the boiling point of the mixture by about 5 °C. The synthesis temperatures were 95 and 100 °C. The resulting samples were used for studying the effect of the drying conditions. The pore size distribution of the sample synthesised at 100 °C was different from the typical distribution of the other samples. For more information on this matter, we refer to Adachi-Pagano et al. [50].

The sample notation takes into account deviations from the typical synthesis conditions given above and is classified as follows: HP = hot plate, B = oil bath, c = closed system, o = open system, EG = ethylene glycol–water mixture, Eth = ethanol refilling, s98 = synthesis temperature raised to 98 °C, d150 = drying temperature 150 °C, N = drying in nitrogen, dry = dried, not calcined, 2C = calcination rate 2 °C/min, redox = after reduction and reoxidation.

2.2. Characterization

Inductively coupled plasma atomic emission spectroscopy (ICP-AES) was used to determine the actual amount of copper, cerium and zirconium after calcination of the precipitated materials. The samples were dissolved in hydrochloric acid before analysis without any visible residues.

Nitrogen adsorption–desorption isotherms were measured using a Micrometrics TriStar 3000 instrument. The data were collected at −196 °C. The *BET surface area* was calculated by the BET equation in the relative pressure interval ranging from 0.01 to 0.30. The *pore volume* was estimated by the Barrett–Joyner–Halenda (BJH) method [70] as the adsorption cumulative volume of pores between 1.7 and 300.0 nm width. This method is based on the assumption of cylindrical pores, and the capillary condensation in the pores is taken into account by the classical Kelvin equation. The pore size distributions were calculated by non-local density functional theory (NLDFT, Original DFT model with N_2 [71], DFT Plus software package [72]) assuming a slit-like pore geometry. For comparison, pore size distributions were also determined with the Harkins–Jura model (cylindrical geometry), a classical method based on the Kelvin equation [73]. Although the models gave different absolute values for the total pore volume, the trends were essentially the same for the samples investigated. For more details on the comparison of DFT and classical models based on the Kelvin equation, we refer to Rouquerol et al. [74] and Chytil et al. [75], and the references cited therein.

XRD data were recorded on a Siemens diffractometer D-5005 (dichromatic Cu $K_{\alpha1+\alpha2}$-radiation). Average crystal size estimates and crystal size distributions for the MMO powders were obtained from a software-based X-ray line broadening analysis (XLBA). The analysis was performed in two steps. Selected experimental XRD fluorite peaks [(1 1 1), (2 0 0) and (2 2 0)] were simulated by means of the software package Profile [76] using the Pearson VII model function. The contribution of Cu $K_{\alpha2}$ to the peak intensities is removed in this step. The program Win-crysize [77], utilizing the Warren–Averbach method [78], was then used to estimate the crystallite size taking into account contributions from microstrain (scaled as mean square root of the average squared relative strain). Contributions from instrumental line broadening were removed using LaB_6 as reference (selected peaks: (1 1 0) at 30.38°, (1 1 1) at 37.44° and (2 1 0) at 48.96°).

Thermogravimetric analysis (TGA) was performed with a thermogravimetric analyser (Perkin-Elmer TGA 7). The device was used to check the metal oxide content in the nitrate precursors, the weight loss of the calcined samples assigned to water/carbonates adsorbed on the oxide powders, and small residues of precursor species not removed after calcination at 350 °C (approx. 1 wt.% at temperatures up to 500 °C). TGA was also used for temperature-programmed reduction and reoxidation (redox). The redox procedure was conducted as follows using crushed oxide powders: (1) pre-oxidation in air up to 500 °C (heating rate: 10 °C/min, dwell: 10 min) in order to remove water/carbonates and precursor residues; (2) cooling down to ambient temperature in air, flushing and stabilization of the baseline, (3) reduction in 7 vol.% H_2 in nitrogen up to 300 °C (5 °C/min); (3) cooling down in H_2/N_2, flushing and stabilization; (4) reoxidation in air up to 350 °C (5 °C/min, 1 h); (5) cooling down in air, flushing and stabilization; (6) reduction in

7 vol.% H_2 in nitrogen up to 300 °C (5 °C/min). The gas flow rate was 80 N ml/min in all steps.

Transmission XAS data were collected at the Swiss-Norwegian Beam Lines (SNBL) at the European Synchrotron Radiation Facility (ESRF), France. Spectra were obtained at the Cu K-edge (8.979 keV) using a channel-cut Si(1 1 1) monochromator. Higher order harmonics were rejected by means of a chromium-coated mirror aligned with respect to the beam to give a cut-off energy of approximately 15 keV. The maximum resolution ($\Delta E/E$) of the Si(1 1 1) bandpass is 1.4×10^{-4} using a beam of size 0.6 mm × 7.2 mm. Ion chamber detectors with their gases at ambient temperature and pressure were used for measuring the intensities of the incident (I_0) and transmitted (I_t) X-rays. The catalyst powder sample was diluted with boronitride. A copper foil, and Cu_2O and CuO powders diluted with boron nitride were used as reference materials. The recorded XAS spectra were energy calibrated, pre-edge background subtracted (linear fit) and normalised using the WinXAS software package [79]. For extended X-ray absorption fine structure (EXAFS) analysis the data were converted to k-space using WinXAS, and the least-square curve fitting was performed with the EXCURVE 98 program [80] based on small atom approximation and ab initio phase shifts calculated by the program.

TEM data were recorded on a JEOL 2010F transmission electron microscope. Small amounts of the catalyst samples were put into sealed glass containers containing ethanol and placed in an ultrasonic bath for a couple of minutes to disperse the individual particles. The resulting suspension was dropped onto a holey carbon film, supported on a titanium mesh grid, and dried. Conventional TEM images were recorded onto a CCD camera. Samples were also examined in scanning transmission electron microscope (STEM) mode, with a nominal probe size of ~0.7 nm. Bright field and dark field STEM images were acquired. Energy-dispersive X-ray spectroscopy (EDS) analysis and mapping were performed using an Oxford Instruments INCA system. Drift compensation was employed to correct for movement of the sample during the time taken for the acquisition of maps.

3. Results and discussion

3.1. General features of the synthesized Cu–Ce–Zr mixed oxides

The colour change from light blue via dark blue/green to green observed during the first 45 min of precipitation is an indication of the heterogeneous nature of the co-precipitation of different metal ions. The pH at which the precipitation of the single metals begins depends on temperature, concentrations and the anions present (see e.g. the titration experiment performed by Lamonier et al. [43] for Cu–Ce mixtures). With urea as the source for hydroxide ions, the formation of carbonate precipitates, which depends on the solubility of the corresponding metal carbonates in aqueous solution as well as the interaction of Cu cations with NH_3, has to be taken into account. This holds especially for rare-earth metals whose carbonates are insoluble in water [81]. In addition, the metal ions may affect each other in respect of their precipitation behaviour. A detailed experimental study, similar to the one performed by Soler-Illia et al. [49] on Cu–Zn basic carbonates, would be necessary to elucidate the reaction path of the nucleation and growth process in the temperature-dependent phase diagram of the Cu/Ce/Zr–nitrate–urea system.

The total (not optimized) yield of precipitation was approximately 80 wt.% based on the nominal oxide composition, including losses due to the post-synthesis treatment.

3.1.1. TEM

TEM images of a calcined Cu–Ce–Zr mixed oxide sample are shown in Fig. 3. Co-precipitation of copper, cerium and zirconium ions results in the formation of nanocrystalline Cu–Ce–Zr

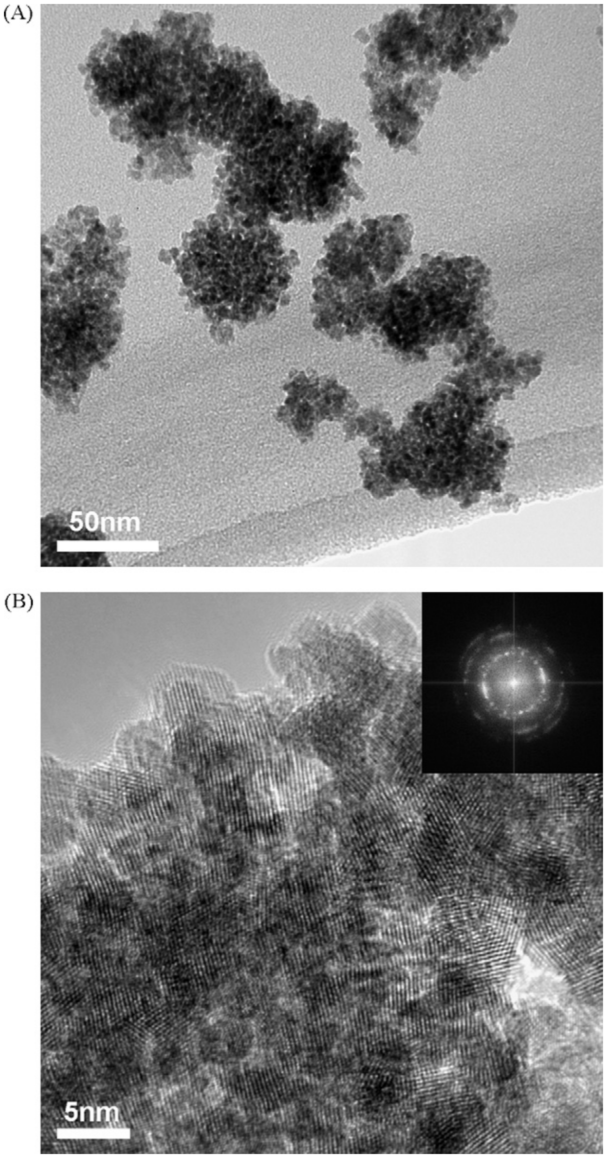

Fig. 3. TEM images of a representative Cu–Ce–Zr mixed metal oxide powder (sample Bo). (A) As calcined sample (scale bar 50 nm). (B) After pre-oxidation (heating rate: 10 °C/min, dwell: 10 min at 500 °C), reduction (up to 300 °C, 5 °C/min) and reoxidation (5 °C/min, 1 h at 350 °C). Scale bar: 5 nm. (Inset) Lattice Fourier transform.

mixed oxide particles. Primary particles formed through nucleation and growth have agglomerated to larger clusters (Fig. 3A), perhaps already during the aging of the precipitate in solution. According to Matijevic [48], the degree of particle agglomeration in solution increases with initial metal concentration. By using lower concentrations of the nitrate precursors, the degree of agglomeration could be reduced and the total surface area of the powder possibly improved. However, particle agglomeration will also occur during drying and calcination. Zhang et al. [82] suggested the addition of an anionic surfactant before drying in order to reduce the degree of agglomeration during drying and calcination.

Fig. 3B displays the crystalline nature of the nanoparticles. A rough particle size estimate lies in the range 3–5 nm. The lattice spacing is visible, and nanocrystalline particles are randomly oriented. The *d*-spacing mainly observed in the individual particles is approximately 3.1 Å, corresponds to the (1 1 1) spacing of the fluorite structure for the CeO_2 and Ce–Zr mixed oxides. The lattice constant is thus estimated to 5.4 Å, in accordance with literature data for Ce–Zr mixed oxides [2,83]. The image of Fig. 3B is obtained after reduction and reoxidation of the calcined sample in Fig. 3A. Comparable images (not shown here) were obtained for the calcined sample, displaying similar features. The fluorite-type structure is therefore preserved upon redox treatment.

3.1.2. XRD

Representative XRD spectra of the Cu–Ce–Zr mixed oxides after different steps in the synthesis are included in Fig. 4. Fig. 4a is recorded after drying at 100 °C. The characteristic peaks of the fluorite-type structure show that this structure is present already after drying. This is in agreement with Hirano et al. [39], who observed the fluorite structure in as-precipitated Ce–Zr (hydrous) oxide samples after drying at 60 °C. Lamonier et al. [43] made a corresponding observation for Cu–Ce mixed oxides dried at 90 °C. No significant change in the fluorite structure can be observed upon calcination (Fig. 4c) and redox treatment (Fig. 4d), in accordance with the TEM images. Fig. 4b will be discussed in Section 3.3. Particle size estimation from XRD data (Table 1, Bo-samples) shows that the particles present after drying of the precipitate are preserved in size after calcination and redox treatment, with a slight tendency towards sintering. Fig. 5 shows the crystal size distribution and the microstrain as a function of crystal size for sample Bo as obtained by XLBA. The average crystal size for this sample is approx. 3 nm (Fig. 5A, Table 1). The primary crystal XLBA size estimate reaches up to 9 nm, with 90% of the particles being smaller than about 6 nm

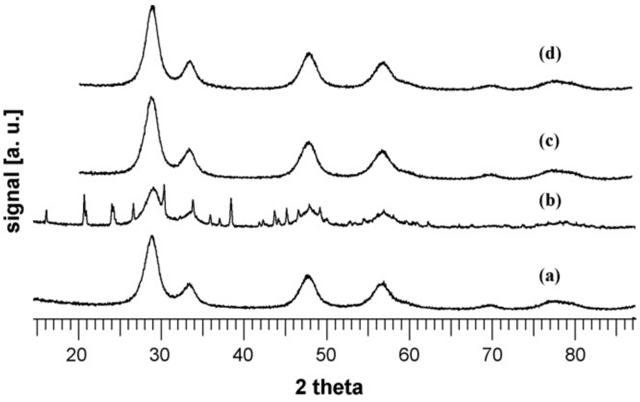

Fig. 4. XRD spectra of Cu–Ce–Zr mixed metal oxide powders at different stages in the preparation: (a) Bo-dry; dried at 100 °C for about 11 h, not calcined. (b) Bo-s98; aging temperature approx. 98 °C. (c) Bo; sample of (a) after calcination at 350 °C for 2 h. (d) Bo-redox; sample of (c) after reduction (up to 300 °C, 5 °C/min) and reoxidation (5 °C/min, 1 h at 350 °C).

Table 1
Surface area, pore volume and primary particle size for the Cu–Ce–Zr mixed metal oxide catalysts

	BET[a] (m^2/g)	stv (m^2/mm^3)	Pore volume		XRD crystal size (nm)
			(cm^3/g)	(cm^3/cm^3)	
Bc	121.13	0.86	0.1347	0.96	
HPo	89.24	0.62	0.1288	0.90	3.1
HPo-2C	89.26	0.62	0.1352	0.95	
Bo	154.42	1.08	0.2678	1.87	3.3
Bo-d120[b]	145.20	1.01	0.2720	1.90	3.8
Bo-2C	163.79	1.15	0.2632	1.84	3.4
Bo-dry					3.1
Bo-redox	141.69	0.99	0.2464	1.72	3.6
Bo-d150	109.34		0.2344		
BoEth	110.49	0.78	0.1943	1.37	5.1
BoEth-dry					4.2
BoEG-s100	170.65	1.19	0.3345	2.34	3.1
BoEG-s100-dry					2.8
BoEG-s100-d250	120.76	0.85	0.2201	1.54	3.5
Bo-s98	115.29		0.1893		3.6

The densities used for calculation of the surface-to-volume ratio (stv) and the pore volume in cm^3/cm^3 (based on the sample volume) are estimated by a linear combination of tabulated densities for CeO_2 (7650 kg/m^3), ZrO_2 (5680 kg/m^3, tetragonal phase) and CuO (6310 kg/m^3).

[a] Estimated error of BET smaller than 5% of the total value.

[b] Catalyst Bo-d120 suffered a temporary temperature hot spot in the initial period of the precipitation, and the drying temperature was approximately 120 °C with a different type of drying furnace applied. XRD profile (fluorite structure only), N_2 isotherm and pore size distribution all similar to those obtained for Bo.

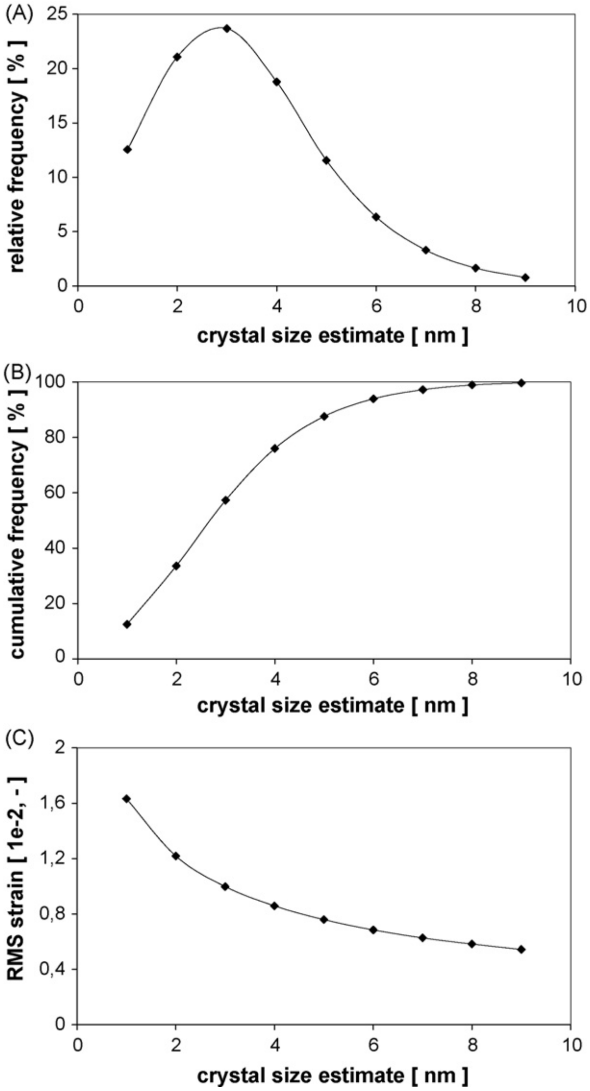

Fig. 5. Crystal size distribution and microstrain (RMS = root mean square) for the Cu–Ce–Zr mixed metal oxide (sample Bo) as estimated from XRD data by means of a software-based X-ray line broadening analysis (XLBA). (A) Relative frequency, (B) cumulative frequency and (C) RMS strain.

(Fig. 5B). The XLBA and TEM results are thus in good agreement. The particles (10%) with size ≤1 nm may, however, be questionable. This is further discussed in Section 3.1.4.

3.1.3. XAS

The XANES profile of a typical calcined Cu–Ce–Zr mixed oxide (sample Bo-d120) at the Cu K-edge is compared with the profile of reference materials: Cu foil, CuO and Cu_2O powder in Fig. 6. The XANES fingerprint of Cu in the MMO resembles that of bulk CuO, indicating a major fraction of the Cu atoms to have a similar structure and oxidation state. The spectral features in the 8978–8985 eV region, namely dipole-allowed $1s \Rightarrow 4p$ transition and 4p–3d hybridization, are indicative of the local symmetry and oxidation state of the average Cu. The position of these transitions is determined from the first inflection point and shifts to increasing energies for higher Cu oxidation state, and Wang et al. obtained from an XANES analysis of $Ce_{0.8}Cu_{0.2}O_2$ that the average Cu in this mixed oxide has a somewhat higher oxidation state than bulk CuO cations [88]. This is similar to Fig. 6, where the energy of the inflection point increases in the order bulk Cu < bulk Cu_2O < bulk CuO < Cu–MMO.

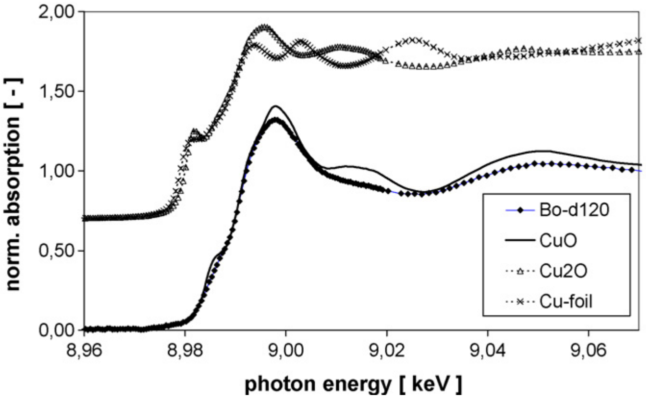

Fig. 6. Normalized Cu K-edge XANES spectra of a typical calcined Cu–Ce–Zr mixed metal oxide powder (sample Bo-d120) and reference materials (Cu foil, CuO and Cu_2O powder). The spectra of Cu_2O and Cu foil are shifted upwards along the ordinate axis for visualisation.

A standard EXAFS analysis (i.e. $k \geq 3$ [54,84]) was performed on the XAS spectra of the same sample. The structural model is limited to the first oxygen shell around the copper atoms. The fitting was carried out in different ways to check whether the structural parameters obtained are sensitive to the fitting procedure: the k-intervals used for fitting were [3;8], [3;9] and [3;12]. For the range k = [3;9], the analysis includes both fitting with k^1- and k^3-weighting in order to account for the high correlation between the coordination number N and the Debye–Waller factor $\Delta\sigma^2$ [84]. In Table 2, the structural parameters obtained by fitting the structural model for the first oxygen shell to the experimental data are shown (R = distance of the oxygen shell to the copper central atom, E_0 = energy shift to correct for deviations from the theoretical edge value). The initial values for the fitting were taken from the crystallographic data for CuO ($E_0 = 0$, $\Delta\sigma^2 = 0.01$). The variance takes into account

Table 2
Structural parameters of the first oxygen coordination shell around the Cu central atom in nanocrystalline Cu–Ce–Zr mixed metal oxide (sample Bo-d120, fitting interval: $\Delta k = 3$–9 Å^{-1}) and the reference compound CuO (k^3 weighting, fitting interval: $\Delta k = 3$–12 Å^{-1}) obtained from a standard EXAFS analysis at the Cu K-edge

	AFAC 0.94			
	E_0 (eV)	R_1 (Å)	N_1	$\Delta\sigma^2$ (Å^2)
Bo-d120	−10.5 ± 1.0	1.92 ± 0.01	2.5 ± 0.5	0.003 ± 0.002
CuO	−15.2 ± 0.8	1.96 ± 0.01	3.9 ± 0.2	0.008 ± 0.001
CuO[a]		1.96	4.0	
CeO_2[a]		2.34	8.0	

The EXCURVE parameter AFAC reflects the amplitude reduction factor. The AFAC value used for fitting the oxide sample was obtained by fitting the reference material CuO with k^3 weighting of the EXAFS function, but deviated only slightly from the theoretical value 1. The parameters given for Bo-d120 result from fitting with both k^1 and k^3 weighting.

[a] Crystallographic data obtained from literature for CuO [101] and CeO_2 [102].

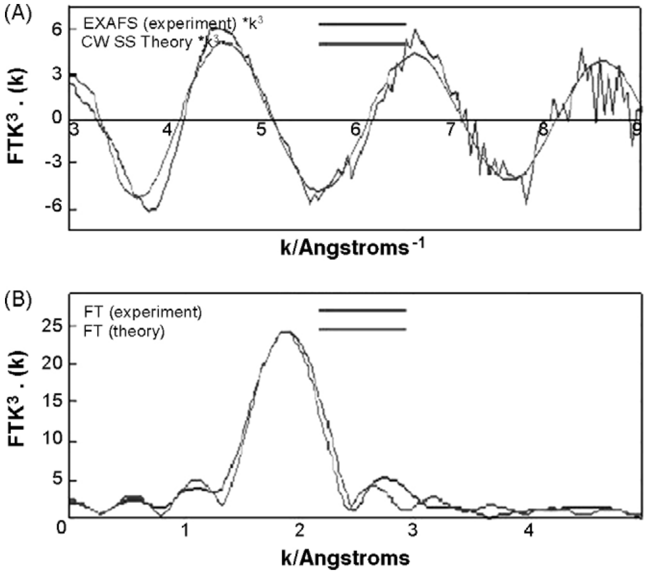

Fig. 7. (A) Cu K-edge EXAFS spectra and (B) corresponding Fourier transforms of a Cu–Ce–Zr mixed oxide catalyst (sample Bo-d120, k^3 weighting, fitting interval: $\Delta k = 3\text{–}9\,\text{Å}^{-1}$), containing both the experimental and the fitted theoretical curve based on small atom approximation. The structural model takes into account the first oxygen shell around Cu.

the uncertainty given by EXCURVE as well as the variation of different fitting approaches. Fig. 7A shows the experimental and theoretical EXAFS spectra in k-space with $k = [3;9]$ and k^3-weighting. The Fourier transform profile indicates that the first oxygen shell is the dominant shell in the experimental EXAFS spectra (Fig. 7B). This is consistent with spectra reported by Shen et al. [24] for Cu–Ce mixed oxides. It is thus reasonable to limit the fitting to the first shell. No significant improvement was obtained by inclusion of further shells.

Table 2 also includes the structural parameters obtained for the CuO reference powder. Here, the coordination number was not included in the fitting procedure (initial value: 4), but was simply refined at the end of the fitting. The structural parameters for the first oxygen shell around the Cu atoms in the mixed oxide are similar to the ones in CuO, in accordance with the XANES comparison. It can therefore be concluded, that the major part of the Cu atoms in the MMO exhibits a similar structural environment as Cu in bulk CuO. Ramaswamy et al. [85] and Lamonier et al. [43] identified different Cu species in electron paramagnetic resonance (EPR) studies on sol–gel prepared, nanocrystalline Cu–Zr oxides and co-precipitated Cu–Ce oxides, respectively. They distinguished framework-substituted Cu ions and extra-lattice species, such as interstitial copper ions or copper dimers, dispersed ions bound to the surface and CuO-type clusters or small particles. The ratio between these species was reported to depend on the amount of Cu in the samples and the temperature pre-treatment. Crystalline CuO, which is not visible to EPR but is to XRD [43], was reported to form at high Cu loadings. Consistent with our XAS results, Lamonier et al. [43] conclude from their EPR studies on co-precipitated Cu–Ce mixed oxides calcined at 400 °C, that a major part of copper exists as CuO-like clusters well dispersed in the solid matrix.

Table 3
Nominal and ICP-AES composition of Cu–Ce–Zr mixed metal oxide catalysts

	Catalyst composition–molar fraction of metals		
	Cu	Ce	Zr
Nominal comp.	0.23	0.54	0.23
Bc	0.10	0.63	0.27
HPo	0.22	0.55	0.23
Bo	0.23 (5)	0.54	0.22 (6)
Bo-d120	0.23	0.54	0.23
Bo-TPR 1	0.16[a]		
Bo-TPR 2	0.20		
BoEth	0.19	0.58	0.23
BoEG-s100	0.22	0.55	0.23

The deviation between the parallel runs was within 5%, and the estimated detection limit is 2000 mg/kg for Ce, 300 mg/kg for Cu and 200 mg/kg for Zr (based on the mass of the sample). The amount of Cu in Bo determined by integration over the TPR peaks obtained in the TGA is also included, assuming as stoichiometry of Cu:O = 1.

[a] The first TPR was reproduced for three freshly calcined samples of catalyst Bo, with the deviation between obtained reduction degrees within 1%.

The reduced coordination number (N_1) of oxygen atoms compared to CuO (Table 2) may relate to the small size of the CuO-like clusters, with a significant number of low-coordinated Cu atoms at the particle surface [53–56]. Neglecting other possible effects [54], a rough estimate for the size of spherical CuO clusters would be 8 Å (with error deviation: 5–15 Å) [55], i.e. in the range of the STEM resolution. However, defects in the oxide structure, such as oxygen vacancies, cannot be excluded. Standard EXAFS analysis tends to underestimate coordination numbers, especially for small particles [54]. Applying the correction function developed by Clausen and Nørskov [54] in a modified form (N-bulk = 4 instead of 12) to our system, the coordination number does not increase significantly. This is only a rough indication, since the correction was developed for metallic copper with fcc structure and not for copper oxide. A multi-data-set EXAFS analysis [56] including asymmetric pair distribution functions for nano-sized particle clusters [54], could further minimize correlation effects.

3.1.4. STEM–EDS

As a result of the nucleation and growth process, the synthesized material should exhibit gradient in composition at the nanoscale. Fig. 8 shows the STEM–EDS elemental mapping of sample Bo-redox. Cu, Ce and Zr are distributed over the whole mapping area (approx. 30 nm × 50 nm), and the average metal composition is close to the ICP-AES-measured composition (Table 3). Within the mapping area, regions of a few nanometres high in Cu or Zr concentration relative to the surroundings could be observed (Fig. 8C and E). This is in agreement with the XAS results (Section 3.1.3) that suggested the existence of CuO-like clusters. As mentioned above, initially formed nuclei probably serve as sites during co-precipitation for the heterogeneous nucleation of a second phase, which grows incorporating different cations at different rates [49]. Thus, the particles should incorporate the three metals in an inhomogeneous way, although governed by their hydrolytic behaviour. Ce and Zr do not necessarily precipitate simultaneously or at the same rate under the

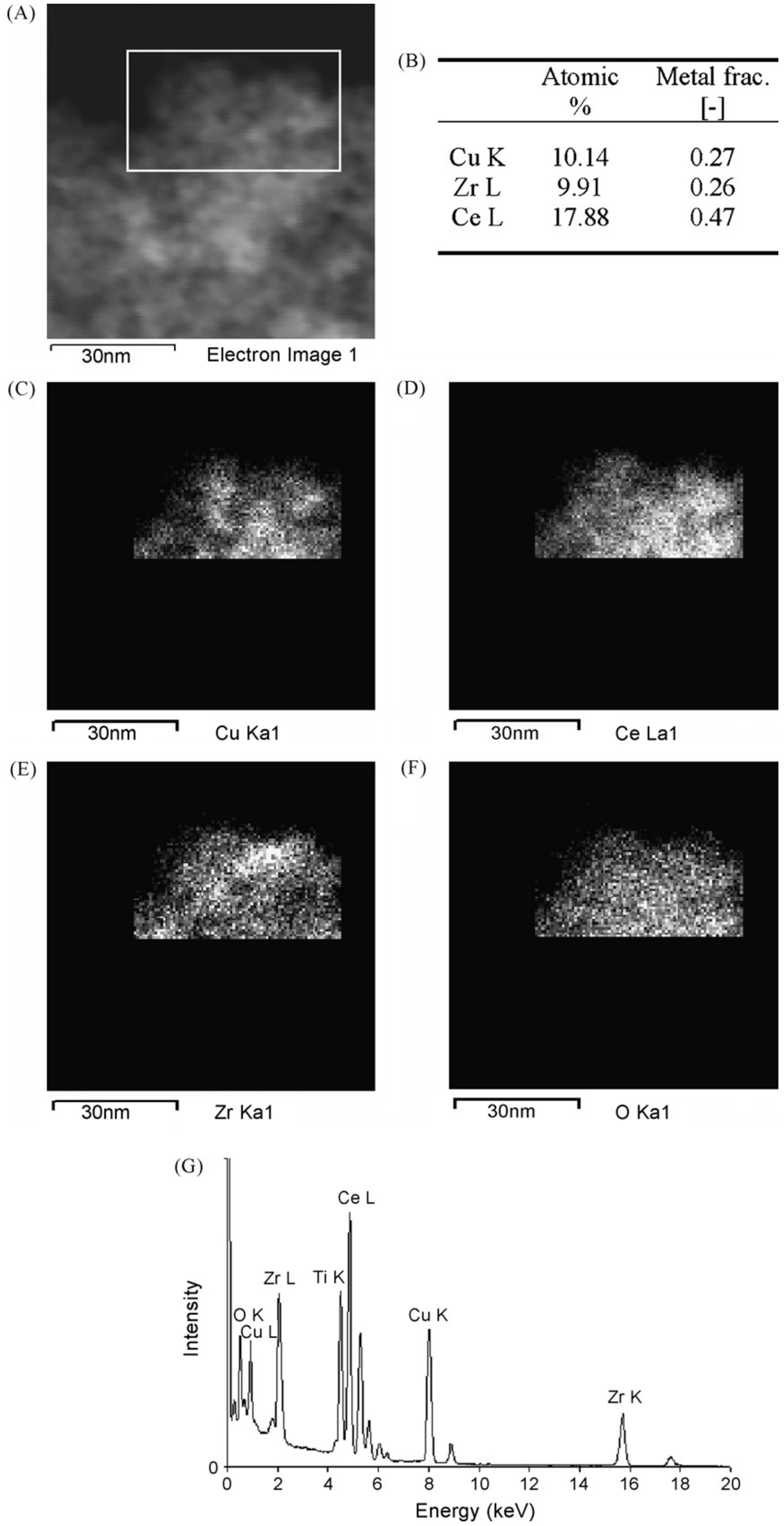

	Atomic %	Metal frac. [-]
Cu K	10.14	0.27
Zr L	9.91	0.26
Ce L	17.88	0.47

Fig. 8. STEM–EDS elemental mapping of a calcined Cu—Ce—Zr mixed oxide powder (sample Bo-redox) after reduction (up to 300 °C, 5 °C/min) and reoxidation (5 °C/min, 1 h at 350 °C). (A) Mapping area, marked with white frame. (B) EDS metal ratio of the mapping area, (C) Cu Kα_1, (D) Ce Lα_1, (E) Zr Kα_1, (F) O Kα_1 and (G) EDS spectrum of the mapping area. Scale bar: 30 nm in all images.

conditions used here (in contrast to the findings in reference [39]) and/or the formation of single element clusters might be more favourable than a homogeneous distribution of all components.

A similar elemental mapping was conducted for sample Bo, i.e. the same material, calcined but before any redox treatment. Inhomogeneous metal distributions at the local scale were found similar to those shown in Fig. 8. Therefore, the redox treatment itself does not significantly change the metal distribution. In situ EXAFS studies on reduction and reoxidation of $Ce_{0.8}Cu_{0.2}O_2$ at 300 °C concluded that the Cu redox process is essentially reversible after one redox cycle [88]. Qi and Flytzani-Stephanopoulos [5] found by XPS analyses of Cu–Ce–La mixed oxides that the amount of surface Cu increased after water-gas shift reaction as compared to the freshly calcined material. Lamonier et al. [43] observed enrichment of Cu at the surface of Cu–Ce mixed oxide particles with increasing temperature. For a discussion on the phase segregation in Ce–Zr mixed oxides under high temperature treatment we refer to Di Monte and Kašpar [2] and references cited therein.

It is known that the lattice parameters (*a*/*b*/*c*) of the crystalline fluorite phase change upon doping of ceria with other metals [2,6,43,46,86]. The corresponding 2Θ-shift in the XRD peaks depends on type and amount of dopant. A powder sample can be considered as a collection of crystallites with different *d*-spacings with a broadening of the XRD peaks as a result of the bandwidth of the *d*-value within the powder. An inhomogeneous composition therefore introduces uncertainty into the determination of particle size from XLBA analysis, since the peak broadening in locally inhomogeneous phases no longer only stems from particle size, strain or the instrument. Based on the TEM images in Fig. 3, it may be assumed that the error introduced is not significant, but the XLBA crystallite size distribution appears to produce somewhat smaller diameters than observed in TEM, down to 1 nm. This phenomenon should not be ignored in quantitative analyses of materials inhomogeneous composition by XRD, and the use of complementary characterization techniques, such as TEM, is advisable.

3.1.5. *TGA-TPR*

The calcination temperature was chosen low enough to avoid sintering of the mixed oxide particles, and high enough to ensure the removal of most of the synthesis residue as gaseous decomposition products (N_2/NO_x, CO_2 and H_2O) from the basic hydrous oxides. The freshly calcined samples were examined by TGA. Temperature-programmed oxidation (TPO, data not shown) confirmed that most synthesis residues were removed upon calcination. A weight loss observed at 100–150 °C can be assigned to adsorbed water and carbonate species [29]. A second weight loss of about 1 wt.% close to 500 °C may correspond to the amount of synthesis chemicals remaining after calcination at 350 °C. Prior to further redox experiments in the TGA set-up, the mixed oxide samples were therefore calcined at 500 °C to eliminate disturbances to the reduction quantification.

Fig. 9 shows the TPR profiles of the calcined Cu–Ce–Zr mixed oxide obtained during redox cycling in the TGA. The maximum of the reduction peak lies at approx. 170 °C with the peak of the second TPR slightly shifted to higher temperatures.

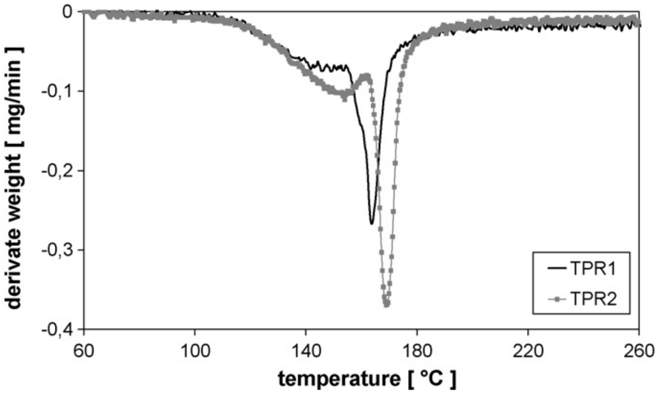

Fig. 9. TPR profiles of a Cu–Ce–Zr mixed metal oxide (sample Bo) obtained during the first (TPR1) and second (TPR2) in the TGA. Between TPR1 and TPR2 the catalyst was reoxidized in air (5 °C/min, 1 h at 350 °C).

This could be caused by densification during the redox treatment, also in agreement with changes in BET and pore volume of samples Bo and Bo-redox in Table 1. Reoxidation of the reduced catalyst after the first TPR step results in a temperature increase of 50–100 °C for 1 g of sample in flowing air at ambient temperature, due to the pyrophoric properties of reduced copper. The temperature range for the reduction peaks observed coincide with reduction temperatures obtained for Cu–Ce mixed oxides prepared by conventional co-precipitation [11,12,46]. The main reduction peaks are found at similar temperatures as for classical Cu–Zn–Al mixed oxide catalysts [29]. While Cu–Ce–Zr mixed oxides have the fluorite structure as the only XRD/TEM-visible crystalline phase, the Cu–Zn–Al systems usually exhibit different oxide phases; Cu/CuO, ZnO, according to XRD as well as (sometimes amorphous) Al_2O_3. Ce–Zr mixed oxides are known to be reducible, but the degree of reduction is low for $T < 200$ °C according to Overbury et al. [87]. A major contribution to the low-temperature reduction stems from the formation of OH-groups at the surface [35]. This can be neglected in TGA because of the marginal weight of hydrogen atoms. The formation of oxygen vacancies by H_2O release would be more TGA sensitive, but plays a significant role above 500 °C only [35]. Addition of reducible metals may improve the low-temperature reducibility of Ce–Zr mixed oxides, but this is also mainly related to the formation of OH-groups [35]. Cu has a moderate effect on the reducibility of ceria [41] that is dependent on the Cu content [42]. In agreement with Overbury et al. [87] and Norman and Perrichon [35], who studied the impact of noble metals, Wrobel et al. [42] found the Cu-promoted reduction of Ce^{4+} to Ce^{3+} in Cu–Ce mixed oxides with $Cu/Ce < 0.5$ to occur mainly above 200 °C. No quantitative discrimination between the formation of OH-groups and oxygen vacancies was made in this study.

With reference to the literature summarized above, we assign the observed reduction of the Cu–Ce–Zr mixed oxide at $T < 200$ °C mainly to the reduction of copper oxide, not taking into account the possible higher oxidation state of Cu in MMO compared to bulk Cu(2+)O discussed in Section 3.1.3. The small, constant weight loss at $T > 200$ °C may originate from the reduction of Ce and possibly to a fraction of less reducible Cu species. The existence of a broad TPR peak with a pronounced shoulder may be related to a stepwise reduction of Cu(2+) via Cu(1+) [42], as well as to the inhomogeneous distribution of copper in the mixed oxide sample, as observed by STEM (Fig. 8). The reducibility of single Cu atoms incorporated in the MMO bulk could be lower than that of surface Cu or Cu particles due to accessibility and/or stability of the oxide state. This interpretation of varying reducibility of different copper species incorporated in the Ce–Zr mixed oxide is in accordance with results obtained by Ramaswamy et al. [85] for nanocrystalline Cu–Zr oxides. They found the extra-lattice species to be reduced more easily than the framework-substituted ions. Consistently, Wrobel et al. [42] reported Cu clusters in Cu–Ce oxides to be more reducible than isolated Cu(2+) ions. However, based on the assumed heterogeneous mechanism of the co-precipitation, also sterical hindrances, i.e. encapsulation of in principal reducible copper species by the Ce–Zr matrix, probably causes variations in the reduction behaviour of copper.

The degree of reduction was quantified by integrating over the low-temperature reduction peaks and assuming a stoichiometry of Cu:O = 1, not taking into account (possible) partial reduction to Cu(1+) [42] or a potentially higher oxidation state of Cu in MMO compared to bulk Cu(2+)O as discussed in Section 3.1.3. The obtained copper content in Bo is given in Table 3 (Bo-TPR-1 and BoTPR-2). Systematic errors may result from the choice of baseline and the simplified reduction stoichiometry. The deviation between the fraction of Cu obtained from TPR-1 (0.16) to that determined by ICP-AES (0.23(5)) indicates that Cu is not completely reduced upon the first TPR. Accordingly, Wang et al. observed an incomplete reduction of Cu in $Ce_{0.8}Cu_{0.2}O_2$ at a reduction temperature of 300 °C [88]. The reduction degree increases upon reoxidation and a second TPR, but even then a small amount of Cu seems to remain in the oxidized state. A similar increase in the extent of Cu reduction from the first to the second TPR was observed for a sample prepared according to the same procedure and, in addition, aged in ethanol under reflux conditions, with a somewhat higher overall reduction degree (TPR-1: 0.18, TPR-2: 0.22). The improvement in accessibility and reducibility of the Cu could be related to changes in the nanostructure of the primary particles upon redox cycling. The segregation of copper atoms to the surface of the mixed oxide particles would be in agreement with XPS results reported by Qi et al. [5] for a used Cu–Ce–La catalyst sample and Lamonier et al. [43] for a high temperature treated Cu–Ce sample. Cu segregation is not necessarily in conflict with our STEM–EDS results, since a slow structural change is not as easily quantified as with XPS. Changes in the local structure around Cu were observed by in situ EXAFS studies on $Ce_{0.8}Cu_{0.2}O_2$ after reduction and reoxidation at 300 °C, but this change was only of a minor extent and the overall redox process was considered essentially reversible after one redox cycle [88].

The enhanced reducibility upon redox cycling was not observed in a Cu–Ce–Zr mixed oxide prepared by a nitrate decomposition method that resulted in two XRD-visible phases (CuO and fluorite, data not shown). Cu–Zn–Al mixed oxides with separate phases (CuO, ZnO, and presumably XRD-amorphous Al_2O_3) also usually reach complete reduction after a single TPR [89]. It may therefore be concluded that the main part of copper in Cu–Ce–Zr mixed oxides prepared by co-precipitation has similar reduction behaviour as in Zn–Al supported systems, whereas a certain part of the Cu is incorporated in the fluorite structure (and/or interacting with Ce atoms [42]) and hence more difficult to reduce. The key factor for such reduction properties appears to be the existence of the fluorite structure, with the improved reducibility interpreted as a sign of segregation within the metastable MMO phase.

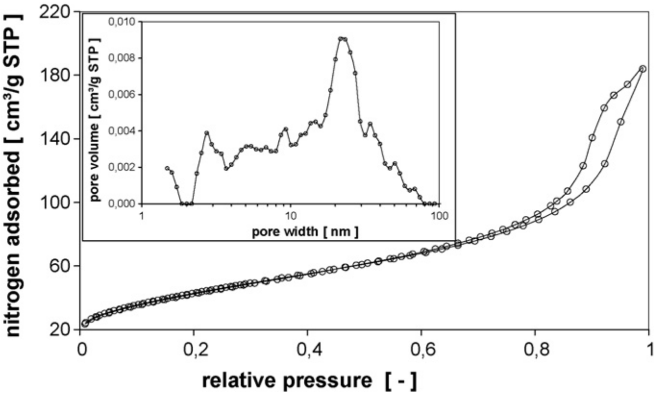

Fig. 10. N_2 adsorption–desorption isotherm of a Cu–Ce–Zr mixed metal oxide (sample Bo) and the corresponding pore size distribution estimated from the adsorption isotherm by NLDFT.

3.1.6. N_2 adsorption–desorption isotherm

Fig. 10 shows a N_2 adsorption–desorption isotherm representative of the Cu–Ce–Zr mixed oxides prepared by co-precipitation. The isotherm exhibits a type-IV character [90] with a hysteresis loop commonly interpreted as a consequence of capillary condensation in the mesopores present in the material [91]. The inset in Fig. 10 displays the pore size distribution of sample Bo obtained by NLDFT analysis of the adsorption isotherm indicating which pore sizes that contribute to the overall pore volume. The pore sizes in the MMO material mainly lie in the mesoporous range (2–50 nm).

3.2. Effect of ammonia

Table 3 shows the composition of some of the prepared Cu–Ce–Zr mixed metal oxides determined by ICP-AES. Bo is representative of an open system (set-up with oil bath) preparation with evaporation and refilling of water. The measured metal composition of Bo corresponds well with the nominal composition based on the amount of precursor salts used. Bo-d120 and Bo were prepared similarly and represent an indication of the reproducibility of the preparation in terms of elemental composition. Bc was prepared under reflux conditions in the same apparatus. Ammonia formed after urea decomposition was not evaporated but remained in the solution under these conditions. As a consequence, ammonia reacts with copper to form complexes that keep a significant amount of copper in solution, while the ratio between Ce and Zr is not significantly affected. An open system is therefore preferred for an optimal utilization of the copper precursor, as well as a straightforward control of the catalyst composition via the initial precursor concentrations.

3.3. Effect of synthesis temperature

Spectrum (b) in Fig. 4 belongs to sample Bo-s98, similar to Bo except the temperature during precipitation and aging being gradually increased to approximately 98 °C. The colour of the precipitate gradually changed from green to dark green/grey. Copper hydroxide is known to decompose to black CuO when boiling in aqueous solution, and may also do so at lower temperature at a lower rate [92,93]. This explains the darkening of the solution when approaching the boiling point of water. The additional XRD peaks could not be ascribed to one, specific compound. Instead, the peaks can be assigned to a mixture of basic copper hydroxide and hydroxynitrate phases, including tenorite (CuO), malachite ($CuCO_3{\cdot}Cu(OH)_2$), azurite ($2CuCO_3{\cdot}Cu(OH)_2$) and gerhardtite ($Cu_2(OH)_3NO_3$) ([93]). These additional phases disappeared after calcination of the dried sample (spectrum not shown), to retain the typical peaks of the fluorite-type structure (such as spectrum (c)).

Sample Bo-s98 has suffered loss of surface area and pore volume compared to Bo (Table 1). This indicates a larger extent of agglomeration of the primary crystallites, since these are of similar size. One may suspect that the formation of intermediate Cu hydroxide species results in a higher degree of Cu segregation in the final MMO, even if a separate CuO phase could not be detected in XRD after calcination at 350 °C. Lamonier et al. [43] investigated Cu–Ce mixed oxides with different Cu loading and related the existence of intermediate copper hydroxynitrates at higher Cu loadings to the appearance of a CuO phase in the calcined MMO.

Sample BoEth (Table 1) was precipitated in the standard way (as Bo), except the gradual addition of ethanol instead of water about 1 h after the onset of the precipitation. The synthesis temperature was simultaneously reduced to the boiling point of the water–ethanol mixture (approx. 83 °C at the end of the synthesis). The aging of the precipitate thus proceeded in boiling solution, and the colour of the suspension changed from green via grey to red-brown in the course of precipitation. This colour change was also observed for precipitation in the water–ethylene glycol solution at 100 °C (BoEG-s100). During washing with ethanol and filtration in contact with air, the colour of the precipitate changed from red-brown to (light) green. The XRD spectra of the dried as well as calcined samples contained only the typical fluorite peaks and no additional phases related to Cu species. BoEG-s100 has lower surface area and smaller pore volume than Bo, as well as a larger primary crystallite size.

The lower Cu content of BoEth (Table 3) is probably caused by the less efficient removal of ammonia at reduced temperature, or a change in the decomposition rate of urea with a change in temperature and solvent. McFadyen and Matijevic [94] also observed a red-brown precipitate during precipitation of colloidal copper hydrous oxide sols from copper nitrate solutions at 75 °C and high pH. The red-brown material, with larger particle size than a blue-coloured mixture of copper hydroxide and hydroxynitrate, was assigned to CuO. Alternatively, the colour change to red-brown could be related to reduction of Cu^{2+} to Cu^{1+}, accompanied by oxidation of ethanol, in analogy with chemical reduction of transition metals by alcohols or polyols. The colour change during washing may thus be interpreted as the reverse redox process.

Synthesis temperatures too close to the boiling point of the solvent apparently have an undesirable effect on surface area and pore volume, and possibly also the homogeneity of the Cu–Ce–Zr mixed oxides. Increasing the temperature during aging enhances the agglomeration of the primary crystallites to give lower pore volume and accessible surface area. Too high temperature during the early stage additionally results in larger crystallites. An optimal MMO preparation requires optimization of synthesis temperature and aging time, parameters that are connected to the pH of the solution via urea decomposition. An elucidation of the reaction path of the precipitation in the temperature-dependent phase diagram of the Cu/Ce/Zr–nitrate–urea system may explain the appearance of additional copper phases in the dried precipitate under some conditions.

3.4. Effect of set-up

According to the ICP-AES data in Table 3, the use of different preparation set-ups had no significant effect on the resulting catalyst composition. HPo was prepared in the simple set-up with the hot plate (Fig. 2A), and exhibits within experimental uncertainty the same metal composition as Bo that was prepared in the oil bath (Fig. 2B).

In terms of structural characteristics (Table 1), Bo has a higher surface area and pore volume than HPo, while the size of the primary crystallites is comparable. Both catalysts have pores in the mesoporous range (2–50 nm, Fig. 10, pore size distributions of HPo not shown), but pores around 20–30 nm are more abundant in Bo than in HPo. The higher mesoporosity of Bo is in agreement with the trend obtained by the BJH method (Table 1). The synthesis set-up therefore affects the agglomeration of the primary particles during aging rather than the formation of the primary particles. Since the time scale for temperature increase, onset of precipitation and change of colour were similar in both set-ups, heat management and hence urea decomposition should be comparable. This may explain why the primary particle formation is unaffected by the choice of set-up.

The agglomeration of the primary particles is presumably affected by the flow field of the synthesis reactor. Different types of stirrers are used in the two set-ups (Fig. 2) that probably create different flow patterns. The flow pattern controls the fluid shear rate acting on the primary crystallites in the solution and hence affects the rate of collisions between the particles. An increase in the average fluid shear rate may decrease the aggregation rate due to reduced contact time between two colliding particles [95]. Hocevar et al. [21] observed an increase in the catalytic activity of Cu–Ce mixed oxides with increasing stirring velocity during co-precipitation. The BET surface area of these oxides was not reported, but beside the effect of enhanced metal distribution, the surface area of the final oxide powder may also be affected. Kunz et al. [96] showed that ultrasonic vibration (US) can be used to enhance mixing during precipitation to give small particles and high-surface area. Thus, an increase in the disruptive hydrodynamic forces acting on the particles in the flow field of

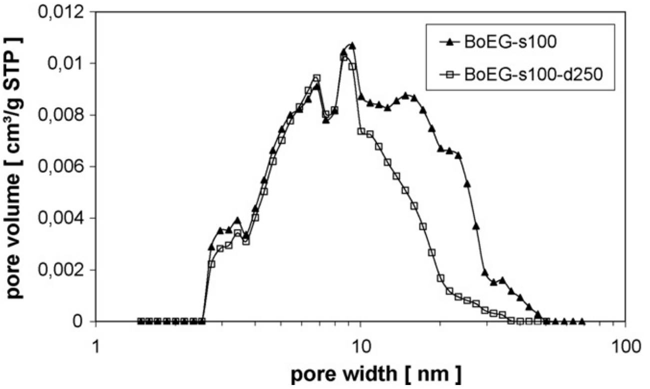

Fig. 11. Effect of the drying temperature on the pore size distribution estimated from the adsorption isotherm by NLDFT. BoEG-s100 was dried at 100 °C whereas BoEG-s100-d250 was dried at 250 °C in air.

the synthesis reactor, by increased stirring, application of ultrasound or use of a set-up with more efficient mixing (increased average fluid shear rate), should slow down the agglomeration of primary particles and lead to a more open pore structure.

3.5. *Effect of drying and calcination conditions*

Several samples were calcined under identical conditions but dried under different conditions. The comparison of sample Bo (drying in static air at 100 °C) to Bo-d150 (drying in static air at 150 °C), as well as BoEG-s100 (drying in static air at 100 °C) to BoEG-s100-d250 (drying in flowing air at 250 °C, heating rate: 5 °C/min) in Table 1 indicates that the drying temperature affects the surface area and pore structure of the subsequently calcined MMO. Increasing the drying temperature to 150 or 250 °C decreases the BET surface area approximately 29% relative to Bo and BoEG-s100, respectively. Fig. 11 shows the pore size distributions of BoEG-s100 and BoEG-s100-d250. The higher drying temperature has resulted in a collapse of pores larger than 10 nm. Pei et al. [97] observed a substantial reduction in pore volume and surface area when increasing the drying temperature from 90 to 250 °C for mesoporous silica prepared by spray drying. A similar, ultrasonic-treated mixed oxide exhibited a decrease of the surface area of about 13% upon drying at 250 °C (flowing air, heating rate: 5 °C/min) relative to 100 °C (static air, 113 m^2/g). The treatment in an ultrasonic bath for 2 h hence resulted in a more dense material with lowered pore volume and surface area already before drying. For more details on ultrasonic treatment we refer to [96].

The pore structure formed by agglomeration during aging in solution is presumably fragile with weak bonds between the primary particles (probably OH-bridge and a few O-bridge). Too high drying temperature may then cause collapse of the structure because of thermal stress and onset of precursor decomposition. The extent of structural collapse depends on the type of material and the preparation conditions prior to drying. Materials with high initial surface area and large pore volume may be more brittle in this context than samples with a dense structure. Drying the precipitates at lower temperature (e.g. 90–100 °C) may facilitate consolidation of the pore structure by strengthening of the bonds between primary particles through a condensation-type reaction that forms oxygen bridges [98], while thermal stress and precursor decomposition are kept at a minimum. The densification during following heat treatment is less pronounced.

The gas atmosphere during drying may also affect surface area and pore volume of the calcined mixed oxide. For the mixed oxide subjected to ultrasonic treatment before drying, drying in flowing nitrogen at 250 °C resulted in 12% higher surface area than drying in flowing air under equivalent conditions. Samples prepared with ethylene glycol and water at 95 °C were dried both in static air at 100 °C (BoEG) and in flowing nitrogen at 250 °C (BoEG-d250N; analog to BoEG-s100-d250, heating rate: 5 °C/min in flowing air). The surface areas were similar despite the different drying temperatures, in contrast to BoEG-s100 versus BoEG-s100-d250. The pore volume of BoEG-d250N is 13% lower than BoEG (0.3031 cm^3/g), as compared to 34% lower for sample BoEG-s100-d250 in flowing air relative to in static air BoEG-s100 (Table 1). The same trend was also found for a sol–gel prepared Cu–Ce–Zr mixed oxide catalyst dried at 150 °C. Drying in flowing nitrogen resulted in 29% higher surface area than flowing air. Xu et al. [99] observed a surface area increase of about 23% for nitrogen-dried ZrO_2 powder pre-calcined at 270 °C compared to the air-dried sample.

The effect of the gas atmosphere should be related to precursor decomposition. For the mixed oxides prepared by co-precipitation, the main decomposition peak in air lies around 200 °C. Using nitrogen instead of air or oxygen may retard the precursor decomposition under elevated temperatures and allow consolidation of the pore structures. At temperatures below the decomposition temperature of remaining precursor compounds, the impact of the gas atmosphere is negligible. This was confirmed by Cu–Ce–Zr precipitate samples dried at 100 °C in static air, flowing air and flowing nitrogen. Approximately the same surface area was measured within experimental uncertainty for all three drying conditions: 123, 119 and 118 m^2/g, respectively.

Bo and HPo were placed directly in a muffle furnace at 350 °C to calcine, whereas Bo-2C and HPo-2C were heated at 2 °C/min up to 350 °C the muffle furnace. Table 1 shows that the heating rate during calcination has a minor effect on pore volume and surface area. Drying at 100 °C for about 11 h seems to sufficiently consolidate the structure to tolerate the different heating rates without significant impact. An increase in the heating rate and hence in thermal stress and rate of precursor decomposition can possibly induce a slight densification of the materials [98]. This would depend on the initial pore structure, however, since large surface area materials with open pore structure appear more susceptible to structural collapse.

3.6. *Comparison with conventional co-precipitation*

Conventional co-precipitation is normally carried out with NaOH or Na_2CO_3 as base. Precursor solution and alkaline solution are prepared separately and then mixed in the precipitation, either by successively adding the alkaline solution to the precursor solution or the other way around. Some selected examples from the literature are

(1) Hocevar et al. [21]: 10 at.% Cu in ceria, base: Na_2CO_3, pH < 5.5, ambient temperature, calcination at 500 °C for 1 h, surface area: 22.5 m^2/g or 0.17 m^2/cm^3 (with the densities given in Table 1).
(2) Liu et al. [6,46]: 10 at.% Cu in ceria, base: NaOH, pH 10, ambient temperature (then 1 h at 90 °C), calcined at 450 °C for 3 h, surface area: 96 m^2/g or 0.72 m^2/cm^3.
(3) Kim and Cha [12]: 20 at.% Cu in ceria, base: NaOH, pH 10, 70 °C, calcined at 500 °C for 5 h, surface area: 91 m^2/g or 0.67 m^2/cm^3.
(4) Shen et al. [24]: 12 at.% Cu in ceria, base: Na_2CO_3, added to precursor, 70 °C, calcined at 350 °C for 12 h, surface area: 191 m^2/g or 1.43 m^2/cm^3.
(5) Lamonier et al. [43]: 17 at.% Cu in ceria, base: NaOH, precursor solution into NaOH solution, start pH 14, 60 °C, calcined at 400 °C for 4 h, surface area: 80 m^2/g or 0.59 m^2/cm^3.

The surface area strongly depends on the method used and not only the calcination conditions. According to the study of Shishido et al. [51] on Cu–Zn oxide catalysts, homogeneous co-precipitation yields catalyst materials superior to the ones obtained by conventional co-precipitation. Conventional co-precipitation can under certain conditions result in surface areas comparable to those obtained by homogeneous co-precipitation (see example (4)). Homogeneous co-precipitation with urea as base precursor allows premixing of all components in the initial solution, and no dosing system is required. Salt and base precursors are mixed on a molecular level in the solution, whereas efficient mixing of salt and alkaline solution during dosing is necessary to minimize concentration gradients for conventional techniques [96]. The use of urea (or ammonia for the conventional technique) as alkaline source facilitates easy removal of the decomposition products, while metal cations from ordinary bases, such as NaOH or Na_2CO_3, might be incorporated into the precipitate and hence affect the properties of the final material.

4. Conclusions

Homogeneous co-precipitation with urea as base precursor results in a Cu–Ce–Zr mixed oxide of composition close to the nominal (0.23:0.54:0.23), as given by the amount of precursor salts in solution. The material exhibits high-surface area (>100 m^2/g) and nanocrystalline primary particles (3–5 nm) composed of a single fluorite-type phase according to XRD and TEM. STEM–EDS elemental mapping shows that Cu and Zr are inhomogeneously distributed throughout the ceria matrix as a result of the heterogeneous nature of the co-precipitation process, and the EXAFS analysis indicates the existence of CuO-like clusters, i.e. similar first oxygen coordination shell distance but lower coordination number, well dispersed in the ceria–zirconia matrix. The XANES results indicate a somewhat higher oxidation state of the average Cu in the MMO compared to bulk Cu(+2)O. We thus assume that both framework-substituted Cu and extra-lattice CuO-like clusters structures exist within the MMO materials.

The amount of CuO-like clusters is dependent on the preparation method and increases with Cu content as well as under heat treatment (sintering). This type of mixed metal oxide materials should therefore not be referred to as homogeneous solid solutions on basis of XRD-based characterization methods, such as XLBA or conventional Rietveld profile fitting, before complementary characterization techniques such as TEM and EXAFS have been applied to confirm that this is actually the case.

Temperature-programmed reduction (TPR) experiments find most of the Cu atoms to be reducible and not inaccessibly incorporated into the bulk, which is important since reduced copper is the active catalyst component in most cases. The reducibility of the mixed oxide improves from the first to the second reduction, between which the catalyst was re-oxidized. We attribute this to improved accessibility of the reducible components (mostly copper) upon heat treatment, as a result of gradual, local phase segregation in the metastable mixed oxide, leading to copper enrichment at the surface. Both XRD and TEM confirm that the crystal structure of the mixed oxide was preserved upon reduction and reoxidation. No phase separation could be detected using these two techniques, which have limitations with respect to local variations in compositions and structure.

The pore structure and surface areas of the mixed oxide catalysts are affected by preparation parameters related to the precipitation stage and the subsequent heat treatment, i.e. drying and calcination. The surface area is governed by the degree of agglomeration of the primary crystallites.

The results and discussion given in this paper are not necessarily limited to Cu–Ce–Zr mixed oxides, but can to some degree apply to other catalyst formulations prepared by co-precipitation, e.g. other single-phase materials such as Co–Ce–Zr, or multi-phase materials such as Cu-, Ni- or Fe-based mixed oxides.

Acknowledgements

This work was supported by the Research Council of Norway through Grant nos. 140022/V30 (RENERGI) and 158516/S10 (NANOMAT). Statoil ASA through the Gas Technology Centre NTNU-SINTEF is also acknowledged for their support. We gratefully acknowledge the project team at the Swiss-Norwegian Beam Lines (SNBL) at the ESRF for their assistance with XAS. Elin Nilsen (Department of Materials Technology, NTNU) is gratefully acknowledged for her assistance with the XRD device.

References

[1] (a) M. Shelef, G.W. Graham, R.W. McCabe, in: G.J. Trovarelli, Hutchings (Eds.), Catalysis by Ceria and Related Materials, Catalytic Science Series, vol. 2, Imperial College Press, London, 2002, pp. 343–376;
(b) D. Duprez, C. Descorme, in: G.J. Trovarelli, Hutchings (Eds.), Catalysis by Ceria and Related Materials, Catalytic Science Series, vol. 2, Imperial College Press, London, 2002, pp. 243–380;
(c) J. Kaspar, P. Fornasiero, in: G.J. Trovarelli, Hutchings (Eds.), Catalysis by Ceria and Related Materials, Catalytic Science Series, vol. 2, Imperial College Press, London, 2002, pp. 217–342.
[2] R. Di Monte, J. Kašpar, J. Mater. Chem. 15 (2005) 633–648.
[3] Y. Li, Q. Fu, M. Flytzani-Stephanopoulos, Appl. Catal. B 27 (2000) 179–191.

[4] E.S. Bickford, S. Velu, C. Song, Catal. Today 99 (2005) 347–357.

[5] X. Qi, M. Flytzani-Stephanopoulos, Ind. Eng. Chem. Res. 43 (2004) 3055–3062.

[6] Y. Liu, T. Hayakawa, T. Tsunoda, K. Suzuki, S. Hamakawa, K. Murata, R. Shiozaki, T. Ishii, M. Kumagai, Top. Catal. 22 (2003) 205–213.

[7] X. Zhang, P. Shi, J. Mol. Catal. A 194 (2003) 99–105.

[8] X.R. Zhang, P. Shi, J. Zhao, M. Zhao, C. Liu, Fuel Process. Technol. 1680 (2003) 1–10.

[9] A. Szizybalski, Ph.D. Thesis, Technical University Berlin, Germany, 2005.

[10] P. Bera, S. Mitra, S. Sampath, M.S. Hegde, Chem. Commun. 10 (2001) 927–928.

[11] T.-J. Huang, Y.-C. Kung, Catal. Lett. 85 (2003) 49–55.

[12] D.H. Kim, J.E. Cha, Catal. Lett. 86 (2003) 107–112.

[13] A. Martinez-Arias, A.B. Hungria, M. Fernandez-Garcia, J.C. Conesa, G. Munuera, J. Power Sources 151 (2005) 32–42.

[14] N.Y. Usachev, I.A. Gorevaya, E.P. Belanova, A.V. Kazakov, O.K. Atal'yan, V.V. Kharlamov, Russ. Chem. Bull., Int. Ed. 53 (2004) 538–546.

[15] G. Avgouropoulos, T. Ioannides, H.K. Matralis, J. Batista, S. Hocevar, Catal. Lett. 73 (2001) 33–40.

[16] G. Avgouropoulos, T. Ioannides, H. Matralis, Appl. Catal. B 56 (2005) 87–93.

[17] X. Tang, B. Zhang, Y. Li, Y. Xu, Q. Xin, W. Shen, Catal. Today 93–95 (2004) 191–198.

[18] P. Bera, S.T. Aruna, K.C. Patil, M.S. Hegde, J. Catal. 186 (1999) 36–44.

[19] Lj. Kundakovic, M. Flytzani-Stephanopoulos, J. Catal. 179 (1998) 203–221.

[20] Y.-J. Wang, X.-F. Dong, W.-M. Lin, Dianyuan Jishu 26 (2002) 134–136.

[21] S. Hocevar, J. Batista, J. Levec, J. Catal. 184 (1999) 39–48.

[22] C. de Leitenburg, D. Goi, A. Primavera, A. Trovarelli, G. Dolcetti, Appl. Catal. B 11 (1996) 29–35.

[23] E.E. Ortelli, J.M. Weigel, A. Wokaun, Catal. Lett. 54 (1998) 41–48.

[24] W.-J. Shen, Y. Ichihashi, Y. Matsumura, Catal. Lett. 83 (2002) 33–35.

[25] C. Lu, W.L. Worrell, J.M. Vohs, R.J. Gorte, J. Electrochem. Soc. 150 (2003) 1357–1359.

[26] S. McIntosh, J.M. Vohs, R.J. Gorte, J. Electrochem. Soc. 150 (2003) 1305–1312.

[27] Y.-J. Wang, X.-F. Jie, X.-F. Dong, W.-M. Lin, Dianyuan Jishu 26 (2002) 43–46.

[28] L. Jalowiecki-Duhamel, A. Ponchel, C. Lamonier, Int. J. Hydrogen Energy 24 (1999) 1083–1092.

[29] M. Rønning, F. Huber, H. Meland, H. Venvik, D. Chen, A. Holmen, Catal. Today 100 (2005) 249–254.

[30] J. Kašpar, P. Fornasiero, J. Solid State Chem. 171 (2003) 19–29.

[31] M. Saito, K. Tomoda, I. Takahara, M. Kazuhisa, M. Inaba, Catal. Lett. 89 (2003) 11–13.

[32] M. Ozawa, J. Alloys Compd. 275–277 (1998) 886–890.

[33] S.-P. Wang, X.-C. Zheng, X.-Y. Wang, S.-R. Wang, S.-M. Zhang, L.-H. Yu, W.-P. Huang, S.-H. Wu, Catal. Lett. 105 (2005) 163–168.

[34] S. Bedrane, C. Descorme, D. Duprez, Catal. Today 75 (2002) 401–405.

[35] A. Norman, V. Perrichon, Phys. Chem. Chem. Phys. 5 (2003) 3557–3564.

[36] A. Suzuki, T. Yamamoto, Y. Nagai, T. Tanabe, F. Dong, T. Sasaki, T. Taniike, M. Nomura, Y. Iwasawa, Proceedings of the 13th International Congress on Catalysis, Paris, France, July, 2004.

[37] M.P. Kapoor, A. Raj, Y. Matsumura, Micropor. Mesopor. Mater. 44–45 (2001) 565–572.

[38] J.P. Breen, R. Burch, D. Tibiletti, in: S.D. Jackson, J.S.J. Hargreaves, D. Lennon (Eds.), Catalysis in Application, Royal Society of Chemistry, Cambridge, 2003, pp. 227–232.

[39] M. Hirano, T. Miwa, M. Inagaki, J. Solid State Chem. 158 (2001) 112–117.

[40] J.A. Wang, M.A. Valenzuela, S. Castillo, J. Salmones, M. Moran-Pineda, J. Sol–Gel Sci. Techol. 26 (2003) 879–882.

[41] Y. Zhang, S. Andersson, M. Muhammed, Appl. Catal. B 6 (1995) 325–337.

[42] (a) G. Wrobel, C. Lamonier, A. Bennani, A. D'Huysser, A. Aboukais, J. Chem. Soc., Faraday Trans. 92 (1996) 2001–2009; (b) C. Lamonier, A. Ponchel, A. D'Huysser, L. Jalowiecki-Duhamel, Catal. Today 50 (1999) 247–259.

[43] C. Lamonier, A. Bennani, A. D'Huysser, A. Aboukais, G. Wrobel, J. Chem. Soc., Faraday Trans. 92 (1996) 131–136.

[44] M. Kurtz, H. Wilmer, T. Genger, O. Hinrichsen, M. Muhler, Catal. Lett. 86 (2003) 77–80.

[45] S. Golunski, R. Rajaram, N. Hodge, G.J. Hutchings, C.J. Kiely, Catal. Today 72 (2002) 107–113.

[46] Y. Liu, T. Hayakawa, K. Suzuki, S. Hamakawa, T. Tsunoda, T. Ishii, M. Kumagai, Appl. Catal. A 223 (2002) 137–145.

[47] Y. Tanaka, T. Utaka, R. Kikuchi, K. Sasaki, K. Eguchi, Appl. Catal. A 238 (2002) 11–18.

[48] E. Matijevic, Chem. Mater. 5 (1993) 412–426.

[49] G.J.A.A. Soler-Illia, R.J. Candal, A.E. Regazzoni, M.A. Blesa, Chem. Mater. 9 (1997) 184–191.

[50] M. Adachi-Pagano, C. Forano, J.-P. Besse, J. Mater. Chem. 13 (2003) 1988–1993.

[51] T. Shishido, Y. Yamamoto, H. Morioka, K. Takaki, K. Takehira, Appl. Catal. A 263 (2004) 249–253.

[52] W.H.R. Shaw, J.J. Bordeaux, J. Am. Chem. Soc. 77 (1955) 4729–4733.

[53] R.B. Greegor, F.W. Lytle, J. Catal. 63 (1980) 476–486.

[54] B.S. Clausen, J.K. Nørskov, Top. Catal. 10 (2000) 221–230.

[55] M. Borowski, J. Phys. IV 7 (1997) 259–260.

[56] A.I. Frenkel, C.W. Hills, R.G. Nuzzo, J. Phys. Chem. B 105 (2001) 12689–12703.

[57] M.V. Twigg, M.S. Spencer, Appl. Catal. A 212 (2001) 161–174.

[58] A. Wootsch, C. Descorme, D. Duprez, Proceedings of the 13th International Congress on Catalysis, Paris, France, July, 2004.

[59] M. Yada, H. Kitamura, A. Ichinose, M. Machida, T. Kijima, Angew. Chem. Int. Ed. 38 (1999) 3506–3510.

[60] T. Bunluesin, R.J. Gorte, G.W. Graham, Appl. Catal. B 14 (1997) 105–115.

[61] T. Bunluesin, R.J. Gorte, G.W. Graham, Appl. Catal. B 15 (1998) 107–114.

[62] D.-H. Tsai, T.-J. Huang, Appl. Catal. A 223 (2002) 1–9.

[63] X. Zheng, X. Zhang, X. Wang, S. Wang, S. Wu, Appl. Catal. A 295 (2005) 142–149.

[64] F.B. Noronha, E.C. Fendley, R.R. Soares, W.E. Alvarez, D.E. Resasco, Chem. Eng. J. 82 (2001) 21–31.

[65] M.K. Dongare, V. Ramaswamy, C.S. Gopinath, A.V. Ramaswamy, S. Scheurell, M. Bruechner, E. Kemnitz, J. Catal. 199 (2001) 209.

[66] A. Mastalir, B. Frank, A. Szizybalski, H. Soerijanto, A. Deshpande, M. Niederberger, R. Schomäcker, R. Schlögl, T. Ressler, J. Catal. 230 (2005) 464–475.

[67] J.C. Vargas, E. Vanhaecke, A.C. Roger, A. Kiennemann, Stud. Surf. Sci. Catal. 147 (2004) 115–120.

[68] F. Schueth, Chem. Mater. 13 (2001) 3184–3195.

[69] J.B. Ko, C.M. Bae, Y.S. Jung, D.H. Kim, Catal. Lett. 105 (2005) 157–161.

[70] E.P. Barrett, L.G. Joyner, P.P. Halenda, J. Am. Chem. Soc. 73 (1951) 373–380.

[71] P.B. Balbuena, K.E. Gubbins, Fluid Phase Equilib. 76 (1992) 21–35.

[72] DFT Plus for Windows, Version 3.00, User's Manual, Micrometrics Instrument Corporation.

[73] W.D. Harkins, G. Jura, J. Am. Chem. Soc. 66 (1944) 1366–1373.

[74] F. Rouquerol, J. Rouquerol, K. Sing, Adsorption by Powders and Porous Solids, Academic Press, London, 1999.

[75] S. Chytil, W.R. Glomm, E. Vollebekk, H. Bergem, J. Walmsley, J. Sjöblom, E.A. Blekkan, Micropor. Mesopor. Mater. 86 (2005) 198–206.

[76] Diffracplus Profile, Profile Fitting Program, User's Manual, Siemens, 2001.

[77] Diffracplus Win-crysize, Crystallite Size and Microstrain, User's Manual, Bruker Analytical X-Ray Systems, 2001.

[78] B.E. Warren, in: B. Chalmes, R. King (Eds.), Progress in Metal Physics, vol. 8, Pergamon Press, London, 1959, pp. 147–202.

[79] T. Ressler, J. Synch. Rad. 5 (1998) 118–122.

[80] N. Binsted, EXCURV98: CCLRC Daresbury Laboratory Computer Program, Daresbury Laboratories, 1998.

[81] F.H. Firsching, J. Mohammadzadel, J. Chem. Eng. Data 31 (1986) 40–42.

[82] F. Zhang, S.-P. Yang, H.-M. Chen, X.-B. Yu, Ceram. Int. 30 (2004) 997–1002.

[83] Y. Nagai, T. Yamamoto, T. Tanaka, S. Yoshida, T. Nonaka, T. Okamoto, A. Suda, M. Sugiura, Catal. Today 74 (2002) 225–234.

[84] D.C. Koningsberger, B.L. Mojet, G.E. van Dorssen, D.E. Ramaker, Top. Catal. 10 (2000) 143–155.

[85] V. Ramaswamy, M. Bhagwat, D. Srinivas, A.V. Ramaswamy, Catal. Today 97 (2004) 63–70.

[86] A.S. Deshpande, N. Pinna, P. Beato, M. Antonietti, M. Niederberger, Chem. Mater. 16 (2004) 2599–2604.

[87] S.H. Overbury, D.R. Huntley, D.R. Mullins, G.N. Glavee, Catal. Lett. 51 (1998) 133–138.

[88] X. Wang, J.C. Rodriguez, D. Hanson, A. Gamarra, M. Martínez-Arias, Fernández-García, J. Phys. Chem. B 109 (2005) 19595–19603.

[89] F. Huber, Z. Yu, S. Lögdberg, M. Rønning, H. Venvik, A. Holmen, Catal. Lett. 110 (2006) 211–220.

[90] S. Brunauer, L.S. Deming, W.S. Deming, E. Teller, J. Am. Chem. Soc. 62 (1940) 1723–1732.

[91] K.S.W. Sing, D.H. Everett, R.A.W. Haul, L. Moscou, R.A. Pierotti, J. Rouquerol, T. Siemieniewska, Pure Appl. Chem. 57 (1985) 603–619.

[92] A.F. Hollemann, E. Wiberg, Lehrbuch der Anorganischen Chemie, 101st ed., Walter de Gruyter, Berlin, 1995.

[93] R.J. Candal, A.E. Regazzoni, M.A. Blesa, J. Mater. Chem. 2 (1992) 657–661.

[94] P. McFadyen, E. Matijevic, J. Inorg. Nucl. Chem. 35 (1973) 1883–1893.

[95] J.-P. Andreassen, M.J. Hounslow, AIChE J. 50 (2004) 2772–2782.

[96] (a) U. Kunz, C. Binder, U. Hoffmann, in: G. Poncelet, J. Martens, B. Delmon, P.A. Jacobs, P. Grange (Eds.), Preparation of Catalysts. Part VI, Elsevier, Amsterdam, 1995, pp. 869–878;
(b) J. Krüger, U. Hoffmann, U. Kunz, ECCE-1 Proc. 2 (1997) 1507–1510.

[97] L. Pei, K.-I. Kurumada, M. Tanigaki, M. Hiro, K. Susa, J. Mater. Sci. 39 (2004) 663–665.

[98] C.J. Brinker, G.W. Scherer, Sol-Gel Science: The Physics and Chemistry of Sol–Gel Processing, Academic Press, London, 1990.

[99] B.-Q. Xu, J.-M. Wei, Y.-T. Yu, J.-L. Li, Q.-M. Zhu, Top. Catal. 22 (2003) 77–85.

[100] Michael Bauccio (Ed.), Primary Literature for ZrO_2: ASM Engineered Materials Reference Book, 2nd ed., ASM International, Materials Park, OH, USA, 1994 (for David R. Lide (Ed.), CeO_2/CuO: CRC Handbook of Chemistry and Physics, 79th ed., CRC Press, Boca Raton, FL, USA, 1998), http://www.matweb.com.

[101] S. Asbrink, L.J. Norrby, Acta Crystallogr. B 26 (1970) 8–15.

[102] M. Wolcyrz, L. Kepinski, J. Solid State Chem. 99 (1992) 409–413.